CHAPTER 4:
TESTING & CHARACTERIZATION OF THE SILICON DRIFT DETECTOR

4.1 Introduction

During the mass production phase of the SVT project, detector tests are performed to evaluate each device in order to select detectors that satisfy the operation requirements [ref. 4.1]. These tests can be separated into two categories: electric tests and drift tests.

Electric measurements, such as resistance values, voltage linearity and anode leakage current are important to determine the quality of the device. Due to the relative simplicity of this type of measurement, they can be performed on probe stations, when the detectors are still part of the initial silicon wafer.

On the other hand, for more sophisticated measurements such as drift curves and temperature dependence, the detector has to be mounted on a special PC board. In this case, the active part of the detector ($6.3 \times 6.3\ cm^2$ square) is laser cut from the original silicon wafer, and glued onto the PC board. The cathodes on both side of the detector are connected to an external voltage divider through wire bonds. The anodes are also connected through wire bonds to pre-amplifier sockets. Once the detector is mounted, it is not simple to disassemble for use in other configurations. Therefore, during the production phase, only a few selected detectors are mounted on PC boards for drift measurements.

In this chapter, I will describe all detector tests used to select the detectors during the production phase. I will first detail the tests structure measurements, followed by the voltage linearity and anode current measurements. In each section, typical results will be presented and the parameters used as selection criteria will be discussed. To illustrate the performance of a typical production batch, I show a summary for each selection test based on a group of 27 STAR-2.9 detectors produced in the same batch.

After the electric measurements, drift non-linearity curves, position resolution and temperature dependence measurements are presented and discussed. These tests were performed on a laser injection test bench.

4.2 Test structure measurements

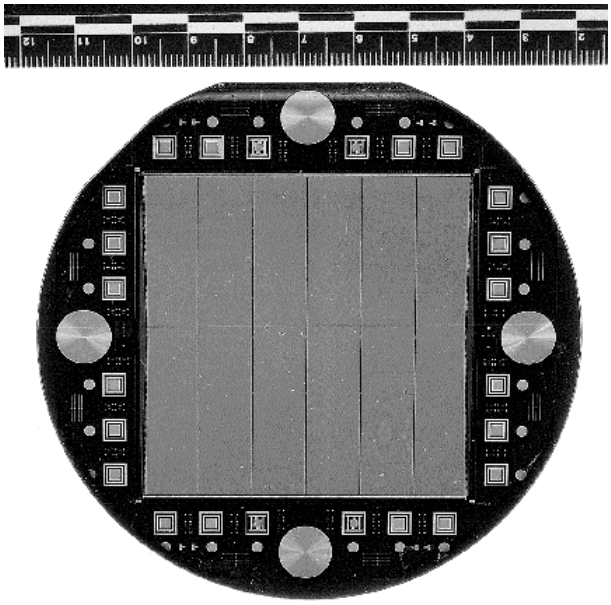

Figure 4.1: *Picture of a silicon wafer after detector processing. The small structures surrounding the detector itself are test structures, such as resistor chains and p-n diodes.*

As mentioned earlier, the detectors are processed on a *4-inch* (*10.16 cm*) diameter silicon wafer. The detector dimensions are $6.3 \times 6.3\ cm^2$. On the outer edges of the silicon wafer, outside of the active area, small testing structures such as resistor chains, p-n diode junctions and MOS capacitors were implemented. Figure 4.1 shows a picture of the uncut silicon wafer after detector processing. A total of 24 sets of test structures are distributed around the actual detector. Figure 4.2 shows a schematic close-up of one type of test structure, a resistor chain.

Measurements from these test structures provide valuable information such as oxide charge density, implanted resistor value, *p-n* junction reverse leakage current and breakdown voltage.

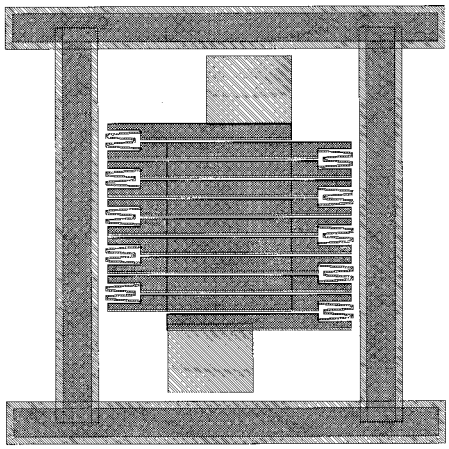

Figure 4.2: *Schematic of the resistor chain test structure. It is composed of 10 implanted resistors identical to the implanted resistors of the detector.*

Measurements are performed on a probe station instrumented with a variable voltage source, a current meter and a capacitance meter. All the electronic devices are controlled by a computer through GPIB standards [ref. 4.2], which allows automated testing of the structures. A pair of single probes makes electric contact with the surface of the test structures for I-V and C-V measurements. A

third probe is used to ground the area surrounding the test structure to eliminate surface currents.

These measurements allow a fast non-destructive diagnosis, which constitutes the first selection criterion for produced wafers with the advantage of not having to probe the active area of the detector itself.

4.2.1 Resistor series test structure

Resistors on the test structures (figure 4.2) have the exact same design as the resistors on the active detector. Each wafer is implemented with eight resistor test structures, four on each side. Each test structure consists of 10 resistors connected in series.

Resistor values are calculated measuring the current as a function of the applied voltage. I-V curves are measured for voltages between $-100V$ and $+100V$. Figure 4.3 shows an example of two typical I-V curves.

The measured resistor value provides information on the concentration of the boron implantation. To pass the selection requirements, the resistance value must be within a predetermined range of values (see figure 4.4). Also, by comparing the resistor values from different test structures on the same wafer it is possible to verify the uniformity of the implantation across the detector.

Notice that for one of the curves shown in figure 4.3, a voltage breakdown occurs at approximately $\pm 80V$. Voltage breakdown values are also a parameter used in the selection criteria. In normal operation conditions, with the detector biased at $1500V$, the voltage drop on individual resistors is approximately $7.0\ V$ (which correspond to $\pm 70\ V$ on the scale of figure 4.3). Therefore the conservative minimum limit for the voltage breakdown value required is $10\ V$ per individual

resistor. Thus, the resistor series in the test structures has to withstand a bias up to *±100V*.

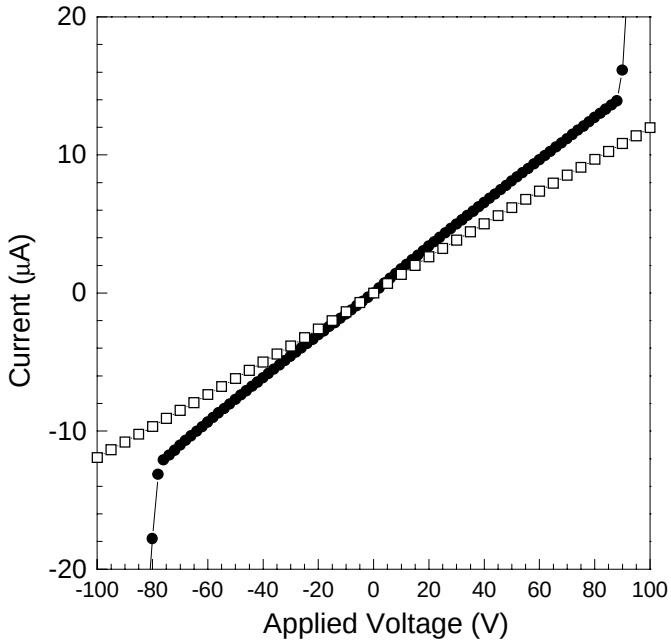

Figure 4.3: *I-V curve from resistor series test structure.*

A summary of the resistance measurement for the group of 27 STAR-2.9 detector prototypes is shown in figure 4.4. The "*x*" axis corresponds to the wafer number while the "*y*" axis corresponds to the resistor value. For each detector there are 8 measurements from the 8 resistor test structures on the wafer. The straight horizontal lines represent the selection criteria limits, which were set to *500 ± 100 kΩ*. These limits were determined empirically, based on results from a large number of detectors that were tested during the development phase of the project. Based on figure 4.4, two out of 27 detectors did not pass the selection criteria.

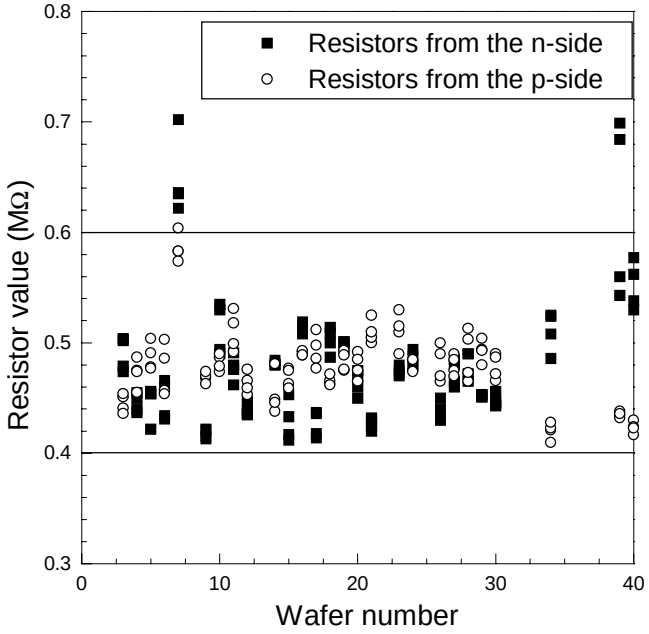

Figure 4.4: *Resistor values measured from the test structures if 27 detectors produced in the same batch.*

4.2.2 p-n Diode junction test structure

A total of twenty *p-n* diode test structures are distributed around the detector. The leakage current through the diode is measured under reversed bias condition. The reverse current through a p-n diode junction [ref. 1.1] can be approximated by the sum of the diffusion component and the generation current component in the depletion region:

$$J_{rev} = q\sqrt{\frac{D_p}{\tau_p}} \cdot \frac{n_i^2}{N_D} + q\frac{n_i W}{\tau_e} + J_{surf} \qquad \textbf{(4.1)}$$

where the first term corresponds to the current from diffusion of the free carriers, the second term corresponds to the contribution from generation currents and the last term is the contribution from possible surface currents. D_p is the diffusion

constant, τ_p and τ_e are the carrier lifetime of holes and electrons, respectively, and n_i is the intrinsic carrier density, which is $1.45\times10^{10}\ cm^{-3}$ for silicon.

At room temperature, the diffusion component is small compared to the second term of the equation. In the design of the diode test structures, a guard ring surrounds the junction to eliminate possible surface currents therefore, the reversed current is dominated by the generation currents. From the 'abrupt junction' approximation, the depletion thickness varies with the applied reverse bias as $V^{1/2}$ (equation 1.18), therefore:

$$J_{rev} = const. \cdot W \approx const. \cdot V^{1/2} \qquad \textbf{(4.2)}$$

A typical I-V measurement from the diode test structures is shown in figure 4.5. The selection criterion for leakage current through the diode is a current of less than *1.0 nA* for reversed bias of *100 V*. This current value corresponds to a carrier lifetime for the electrons of approximately *11 ms*, for *3.0 kΩ·cm* silicon at room temperature. Currents lower than *1.0 nA* correspond to a longer carrier lifetime. The diode current measurement provides information on the carrier lifetime and on the quality of the detector processing. The criterion was defined to assure that the expected leakage current of the detector is relatively low and the carrier lifetime is longer than the longest drift time (~5μs).

Several effects can cause high leakage current through the diode. Impurities during the high temperature steps of the detector processing (sintering, annealing) can be diffused into the silicon and generate deep carrier levels that would lower the carrier lifetime and increase the leakage current. Also, impurities during the photolithography step can cause 'pinholes' in the implantation and create an electric 'short' through the diode.

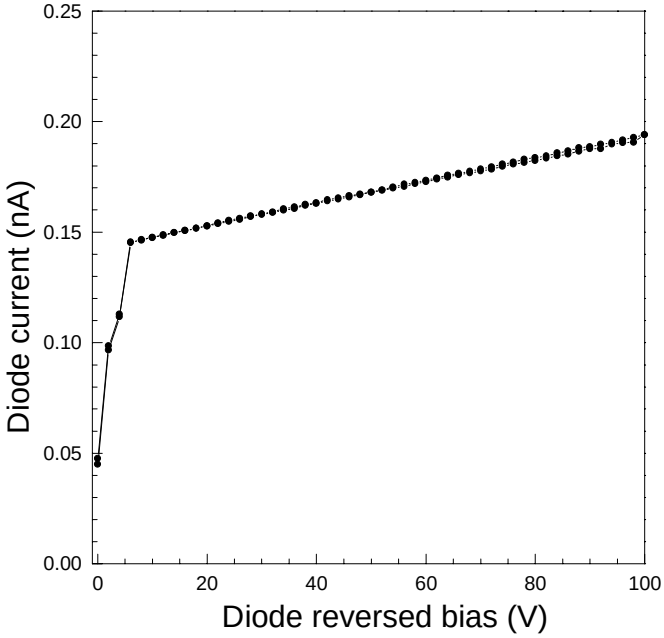

Figure 4.5: *I-V measurement from one of the p-n diode junction test structures mounted on the side of the silicon wafer, near the detector.*

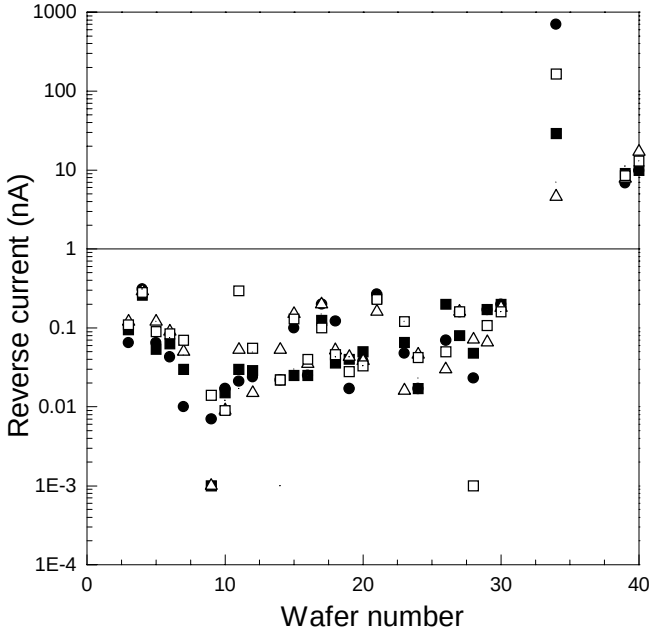

Figure 4.6: *Diode test structure current measured at reversed 100V as a function of wafer number. The horizontal line indicates the selection criteria limit of 1 nA.*

Figure 4.6 shows results from diode leakage current measurements for the 27 test detectors. On each detector wafer, 4 diodes were measured with a reverse bias of *100V*. Based on the measurements, 4 of the 27 detectors do not satisfy the test requirements, corresponding to a yield of 85%.

4.2.3 p-n junction capacitance measurement

Under reversed bias condition, a *p-n* junction acts as a parallel-plate capacitor with permittivity $\boldsymbol{\varepsilon}$ and plate separation given by the depletion thickness (W). For a junction of area $\boldsymbol{A}$, the capacitance is given by:

$$C = \varepsilon \frac{A}{W} \tag{4.3}$$

Substituting the depletion thickness formula from equation 2.18, the capacitance dependence on the applied voltage can be written as:

$$\frac{1}{C^2} = \frac{2}{q\varepsilon N_D} \cdot \frac{1}{A^2} \cdot V \tag{4.4}$$

Figure 4.7 shows a typical result from a capacitance measurement as a function of reverse bias. As expected, a linear dependence is observed. From the slope of this curve it is possible to calculate the doping concentration (N_D) of the silicon. However, this measurement is not sufficiently sensitive to determine the doping concentration accurately. Diode junctions with larger area have higher capacitance values providing better accuracy for calculating the doping concentration through this method.

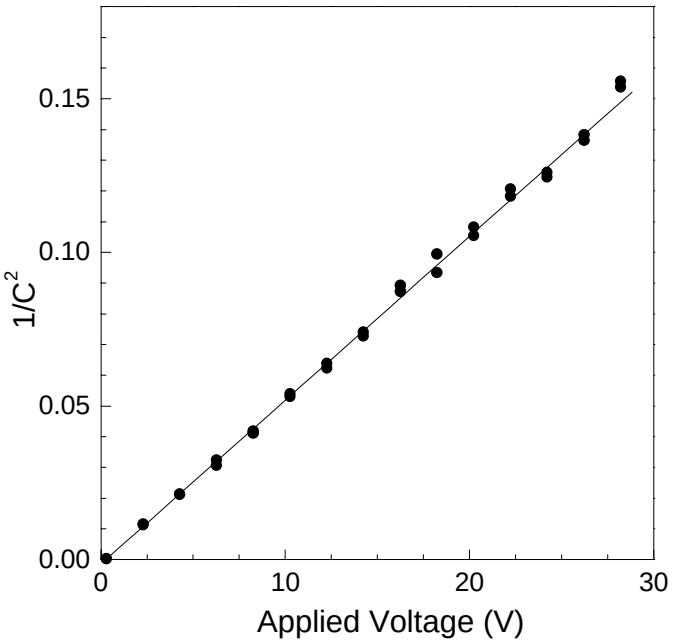

Figure 4.7: *$1/C^2$ versus reverse applied voltage of a p-n diode junction.*

4.2.4 MOS capacitor test structure

In addition to the diode and the resistor test structure, a simple metal overlay on the oxide provides a MOS capacitor. Measurement of the flat band voltage shift [ref. 4.3] of the MOS capacitor yields information on the oxide quality, which is determined by the density of charges fixed at the *Si-SiO_2* junction. The better the oxidation process the lower the density of fixed charges.

Figure 4.8 shows measurements of flat-band voltage shifts from the MOS capacitors on two different silicon wafers. For positive applied voltage, the capacitance is determined by the oxide thickness ($C_{ox} = \varepsilon_{ox}/d$). For negative voltages, the capacitance decreases as a depletion layer underneath the metal overlay forms and increases. The capacitance at large negative value saturates with applied voltage, and can be viewed as two capacitors in series, the oxide

capacitance and the depletion layer capacitance. Due to the fixed positive charges of the *Si-SiO₂* interface, the flat-band voltage is shifted towards more negative values. In figure 4.8 the values of the flat band voltage shift measured for two different detectors from different production batches are *–1 V* and *–5.5 V*. These are typical values for a good and a bad flat-band voltage shift, respectively. The voltage shift is proportional to the density of the fixed oxide charges, therefore a low value of the flat band voltage shift is desired for a good *Si-SiO₂* junction. The fixed oxide charges affect the potential distribution near the surface of the detector, as will be discussed in more detail in the next chapter.

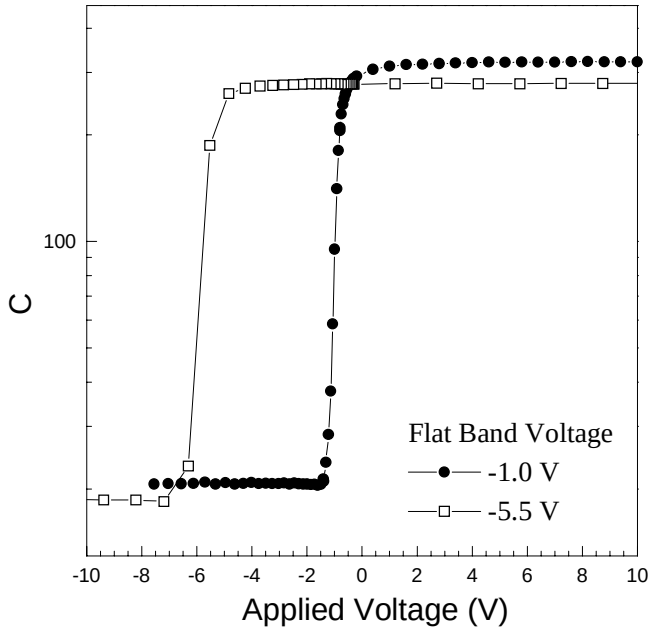

Figure 4.8: *C-V characteristics of a MOS (metal-over-silicon) capacitor, at high frequencies.*

4.3 Properties of the active wafer

Up to this point, only the peripheral test structure area of the detector was tested. In the next step of the procedure, the active part of the wafer, the actual detector itself is tested.

Electrical measurements are performed with the detector wafers mounted on a special testing probe station. Figure 4.9 shows a picture of a detector wafer mounted on the station. Probes on both sides of the detector make electric contact with the surface of the detector, biasing the cathodes. The cathode probes are special PC cards that connect to an external voltage divider. On the anode side a 60-probe card is mounted to measure the anode leakage current. The probe cards are aligned to the detector with the help of microscopic X-Y stages and an optical microscope. By moving the anode card several times, all 240 anodes on one side of the wafer can be tested.

On the probe station, the detector is biased up to *-1000V*. Voltage linearity and anode leakage currents are measured. With this probe station, the active area of the detector can be tested without actually bonding the detector onto an electric PC board.

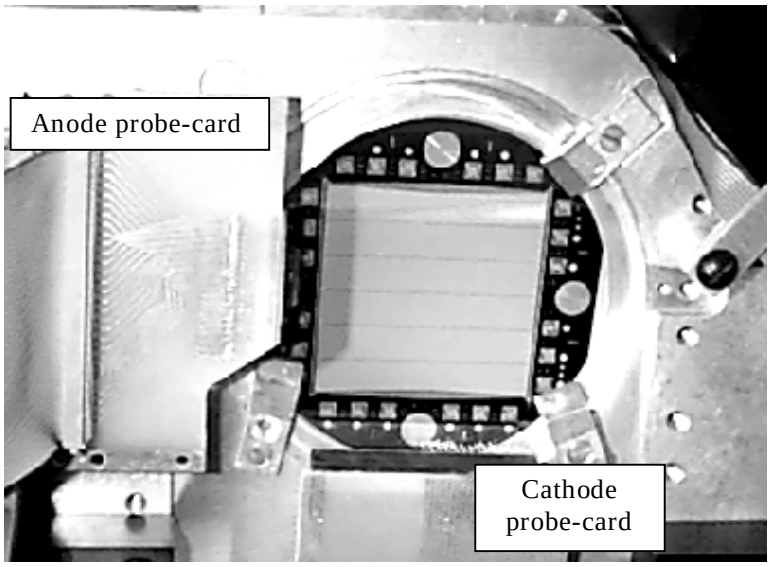

Figure 4.9: *Picture of a detector wafer mounted on the probe testing station. Mounted on the left side, is the anode probe card, making contact with 60 consecutive anodes. On the bottom side, and also on the opposite surface, not shown in this picture, are the cathode probes.*

4.3.1 Voltage linearity

Before presenting the results of the voltage linearity measurements, I discuss the correlation between the voltage linearity and the drift non-linearity. Simulation results of the potential distribution in the drift region illustrate the effect of voltage non-linearities on the drift velocity. From this correlation, limits for the voltage non-linearity were determined and used as selection criteria.

4.3.1.1 Correlation between the voltage linearity and the drift non-linearity

For a drift distance "*x*", the drift non-linearity is defined as:

$$\Delta t(x) = t(x) - t_0(x) = \int_0^x \frac{1}{v(x')} \cdot dx' - \frac{x}{v_0} \qquad \textbf{(4.5)}$$

By this definition, the drift non-linearity corresponds to the deviation of the measured drift time from the drift time for a constant velocity. Several factors such as temperature non-uniformity across the detector or localized impurities can cause a variation on the drift velocity of the electrons. To estimate the intrinsic non-linearity of the drift detector, we will consider only the non-linearity correlated to the non-uniformity of the electric field. As mentioned before, the drift velocity is proportional to the electric field as:

$$v_{drift} = \mu_{Si} \cdot E_{drift} = \mu_{Si} \cdot \frac{dV}{dx} \qquad \textbf{(4.6)}$$

where, "μ_{Si}" is the electron mobility in the material (*1350 cm^2/V-s* for silicon at room temperature) [ref. 1.1]. In this case, the drift-non-linearity can be written as:

$$\Delta t(x) = \frac{1}{\mu_{Si}} \int_0^x \left(\frac{1}{\frac{dV}{dx'}(x')} \cdot dx' \right) - \frac{x}{v_0} \qquad \textbf{(4.7)}$$

which allows correlating the drift-non-linearity to the voltage non-linearity.

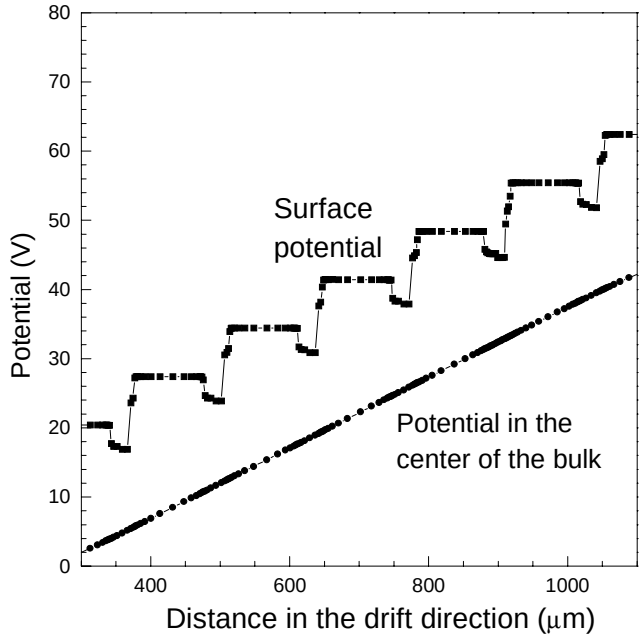

Figure 4.10: *Voltage distribution along the drift direction (Y) for Z=0 (detector surface) and Z=140μm (center of the bulk).*

Any voltage non-linearity in the cathodes at the detector surface will be attenuated inside the bulk. Figure 4.10 shows the simulated potential distribution at the surface of the detector and at the center of the detector bulk, where most of the electron drift occurs. It was calculated using the same simulation package used to calculate the potential distribution of the anode region shown in chapter 3 [ref. 3.14]. Due to the finite size of the cathodes and the gap between them, the potential distribution at the surface is not gradually linear. However, this effect

attenuates in the detector bulk, leading to a non-linearity smaller than *0.02 V/μm*. Figure 4.11 shows the deviation from a linear fit of the potential distribution at the center of the detector bulk as a function of drift distance. The solid circles represent the voltage non-linearity for the normal distribution shown in figure 4.10. To estimate the effect of the voltage non-linearity, potential distributions were calculated forcing a voltage non-linearity of *5 V* and *10 V* on one of the cathodes, at the surface of the detector.

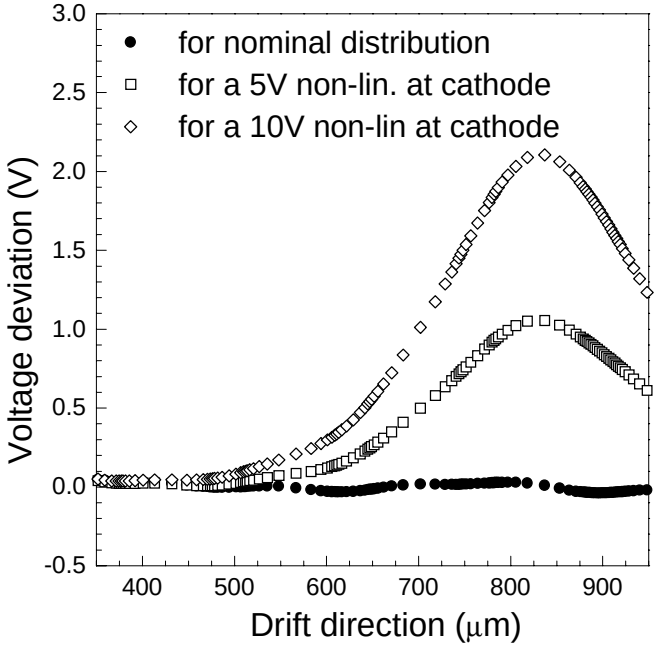

Figure 4.11: *Voltage non-linearity in the center of the detector bulk. The solid circles correspond to the voltage non-linearity of the nominal potential distribution. The curves with open squares and solid triangles correspond to the voltage non-linearity for the case when there is a 5V or 10V non-linearity in the cathode.*

Based on the voltage distributions in figure 4.11, the drift-non-linearity can be calculated using equation 4.7. Results are shown in figure 4.12, assuming a detector at room temperature (300K).

For the nominal voltage distribution, the voltage non-linearity in the detector bulk is smaller than *20mV/μm*, which corresponds to a drift non-linearity better than *0.2ns*. With a *6.2μm/ns* drift velocity (*500 V/cm*), the drift non-linearity thus translates to an error in the position determination of *1.2μm*. This is the intrinsic resolution of the drift detector, due to the voltage non-linearity in the bulk caused by the finite size of the cathodes. A voltage non-linearity of *5V* or *10V* measured at the cathodes corresponds to a position non-linearity of approximately *17 μm* and *35 μm* in the region of the voltage non-linearity, respectively.

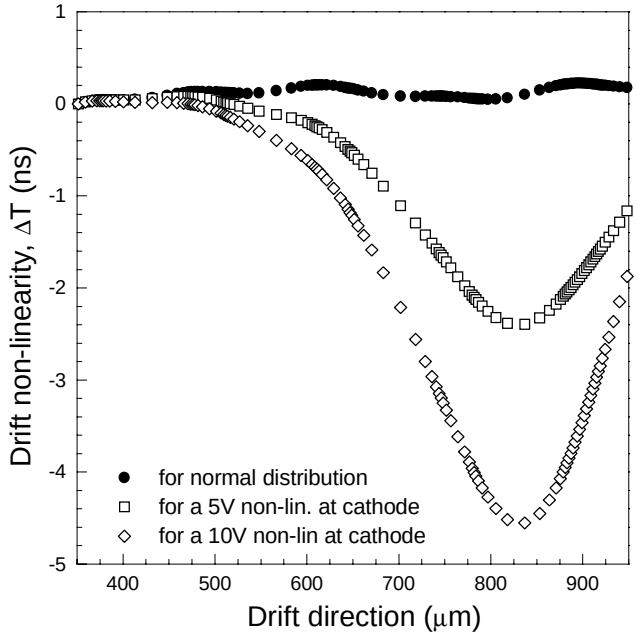

Figure 4.12: *Calculated drift non-linearity as a function of drift distance.*

The non-linearities discussed above are fixed for each detector and they do not vary in time. Therefore, they can be mapped out and a better position determination can be achieved. Mapping of drift time as a function of drift distance is achieved with a laser setup, which will be discussed in section 4.4.

4.3.1.2 Voltage measurements from the probe station

As mentioned earlier, the detector bias on the probe station is applied in the same fashion than in the experiment, where every 10^{th} cathodes is connected to an external voltage divider. The maximum applied voltage is kept at *-1000 V* due to probe-card breakdown limits. Experience from previous measurements has shown that voltage non-linearity can be detected, even if only every 10^{th} cathode is measured. Based on the drift non-linearity calculations presented in the previous chapter and on statistics from earlier measurements, the acceptable limit for voltage non-linearity was set to *±2.0 V*. Figure 4.13 shows a typical output graph from the probe-station measurements. The cathode voltages are measured for 5 different bias voltages.

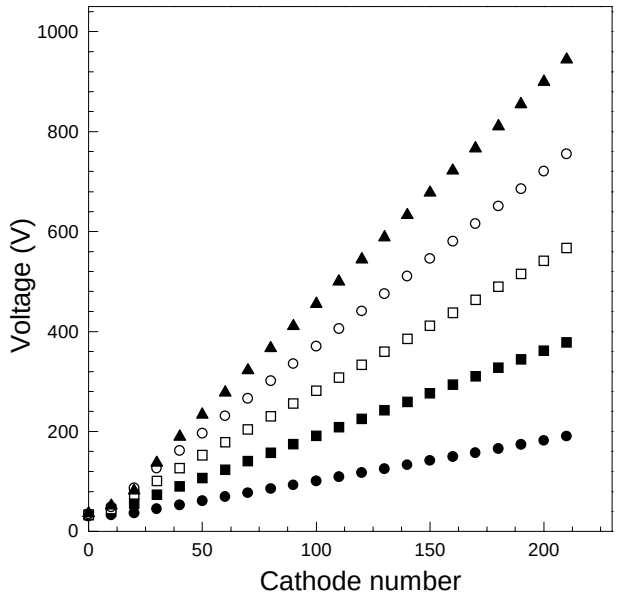

Figure 4.13: *Typical voltage distribution measured with the probe-station.*

From the group of 27 detectors used to illustrate the selection criteria, all detectors had voltage non-linearities below the limit of *±2.0 V*. These results confirm the improvement of the detector performance due to the changes made from the STAR-2.7 prototype to the final STAR-2.9 prototype.

4.3.2 Anode leakage current

DC current in the anodes introduces electric noise into the signal output. Several sources can contribute to this anode leakage current, such as thermally generated electron-hole pairs originating from recombination and trapping centers in the detector bulk. These centers can be caused by lattice irregularities and doping impurities. Generation current due to impurities and lattice irregularities can be as high as a few $\mu A/cm^2$. A second contribution to the anode current is the reversed leakage current of the cathode p-n junction. Anode currents from the cathode junctions can be estimated from the diode test structure currents and are expected to be lower than *1 nA* for each anode. In general, surface currents are the biggest contribution to the anode currents. However, in the STAR drift detector, the "E1" electrode that surrounds the anodes keeps the surface currents from entering the anodes. The surface currents are collected in the guard anode that is placed behind the anodes.

The pre-amplifier/shaper circuit developed for the final SVT was designed to be operated with DC input current below *150 nA*. Therefore, *150 nA* is the leakage current limit acceptable for a detector. Above *200 nA*, the positions resolution starts to degrade gradually, and at *1* μA, the pre-amplifier/shaper saturates. Most of the "good" detectors from the STAR-2.9 design have a base-line current value below *10 nA*. Figure 4.14 shows some typical anode leakage currents measured on the probe station. Measurement from 60 anodes are shown for three different detectors, where two of the detectors (#03 & #10) satisfy the selection criteria, whereas the third one (#23) has a high leakage current area that leads to detector rejection. The original SVT specification allows a maximum of 2% bad channels, therefore the detector leakage current criterion, requires that 98% of the anodes of the detector (470 anodes), have leakage current below *150 nA*.

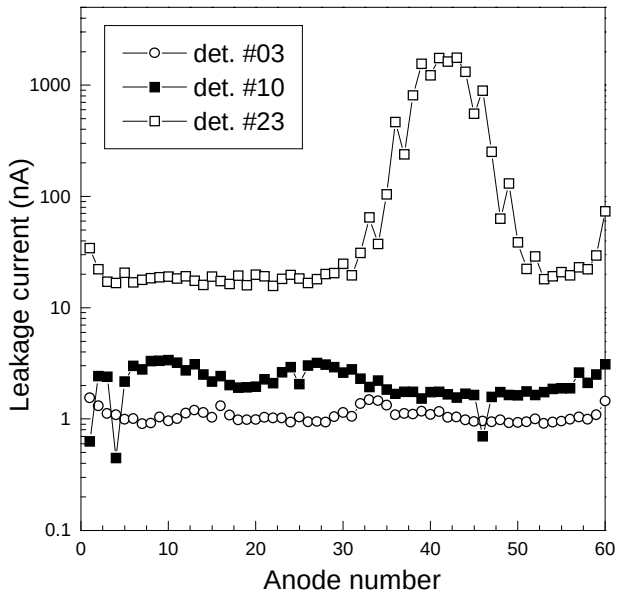

Figure 4.14: *DC current measurement for 60 anodes from three different detectors.*

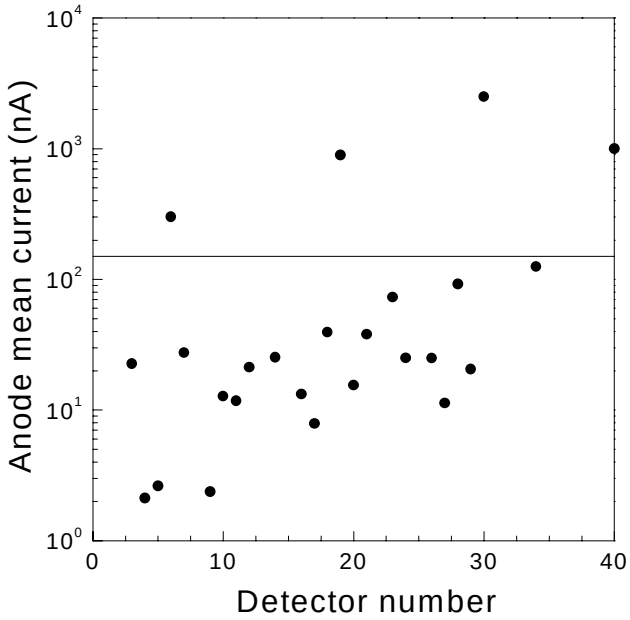

Figure 4.15: *Summary of the anode leakage current measured on the probe station, with the detector bias at 1000V.*

Figure 4.15 shows a summary of the anode leakage currents for the 27 detector control group. Open squares represent the averaged value of the measured anodes for each detector and the solid circles are the mean value of the highest *10%* values measured on the same detector. Four of 27 wafers do not pass the requirement.

4.3.3 Summary of the testing procedure

The active part of the silicon drift detector occupies most of the silicon wafer, as seen in figure 4.1. In silicon based devices the production yield reduces proportionally with the area of the device. As an example, for small electric IC's, such as the SVT pre-amplifier IC's (described later in chapter 7), up to 600 IC's are produced in a single silicon wafer. Most of the silicon wafer processing irregularities are localized, therefore only the chips located in that region are lost and still a considerable number of “good” chips are produced in a single silicon wafer. In the case of the STAR silicon drift detectors, small localized defects on the silicon wafer affect the overall performance of the detector.

For the SVT project a large number of detectors is required, therefore it is important to verify that every detector to be mounted meets specifications. Dead areas on the detectors considerably reduce the tracking efficiency, and replacement of single wafers in the completed SVT detector will be very difficult.

Based on the tests discussed in the previous sections, it is possible to determine the quality of the detector wafer in a non-destructive manner and assure that the selected wafers will perform as expected. From the 27 detectors tested, 7 detectors have measurements beyond the criteria limits, the remaining 20 wafers satisfy all requirements corresponding to a production yield of 74%. For the SVT, up to 600 detector wafers will be produced. A *70%* production yield corresponds to a total of 420 “good” wafers, which is far more than the 216 wafers needed for

the SVT. Should the yield of the first batch of final wafers repeat itself in subsequent submissions, the number of produced wafers will be reduced accordingly. Presently, wafers are produced commercially. Each production batch starts with 125 uncut NTD wafers.

4.4 Drift measurements with the laser

Once the wafers are tested on the probe-station, the active detector area is "cut" from the circular wafer using a high intensity infrared laser, then most of the selected wafers are mounted onto the ladder configuration to be used in the SVT. Detector ladders will be composed of 4, 5 or 7 detectors each. Once mounted on the ladder, each detector will be tested with a laser for drift non-linearities and position resolution. In the remainder of this chapter, drift measurements performed on detectors mounted on PC boards will be discussed. These tests are essentially the same tests to be performed on the SVT ladders to calibrate the detectors and they were also used to characterize the detectors during the development phase.

Figure 4.16 shows a representation of the laser test station setup. Laser light is used to simulate a charged particle hitting the detector. Two types of lasers were used for drift measurements: a solid state diode laser with wavelength of *921 nm* that only ionizes the surface, and a Nd:YAG laser with *1060 nm* wavelength that penetrates the silicon and leaves a 'line' of ionization in the detector, comparable to an ionizing charged particle. A stepping motor controlled X-Y table capable of sub-micron step sizes was used to position the laser on the detector. The laser is focused onto the detector through an objective of a microscope yielding a small ($\approx 20\mu m$ wide) spot size.

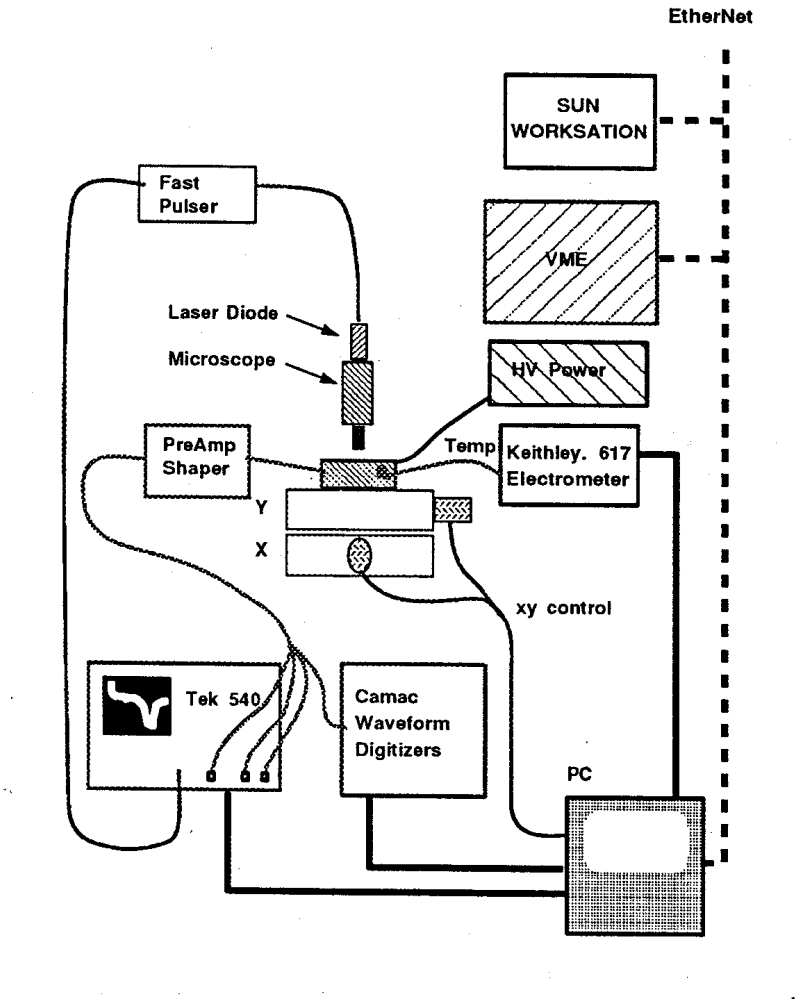

Figure 4.16: *Schematic layout of the laser test station used for drift measurements.*

The signal from the anodes is readout through a pre-amplifier/shaper circuit and digitized by a fast waveform oscilloscope. A computer is connected to the X-Y table and the oscilloscope so that the measurements are automated and the data is stored in a readable format.

For drift linearity measurements, the laser was set to high intensity, with the output signal amplitude equivalent to several (up to 10 times) minimum ionizing particles (MIP's) to reduce the influence of the background noise. For intrinsic position resolution measurements, the laser amplitude was kept low, near a MIP signal to simulate a more realistic event.

4.4.1 Electron cloud drift parameterization

Electrons produced by an ionizing particle crossing the detector drift towards the center of the detector bulk forced by the parabolic component of the electric field. The electron cloud will be confined to the center plane while it drifts towards the anodes. Therefore the shape of the electron cloud can be approximated by a two dimensional gaussian:

$$Q(x,y,t) = \frac{Q_0}{2\pi\sigma_x\sigma_y} e^{-t/\tau} e^{-(x-x_0)^2/2\sigma_x^2} e^{-(y-(y_0-v_{drift}t))^2/2\sigma_y^2} \quad \textbf{(4.8)}$$

where Q_0 is the total electric charge, "y" is the distance from the anodes in the drift direction and "x" is the distance in the transverse direction. "x_0" and "$(y_0 - v_{drift}t)$" are the coordinates of the center of the electron cloud and "σ_x" and "σ_y" are the width of the electron cloud in both directions. The first exponential term of the equation corresponds to the charge recombination effect where "τ" is the recombination constant. Considering a "good" detector, with a low density of charge trapping centers, the lifetime of the electrons in the bulk is relatively high, on the order of milliseconds. Therefore, the recombination effect term can be neglected to first approximation.

4.4.1.1 Signal amplitude as a function of drift distance

The shape of the signal (amplitude and width) measured in a single anode is determined by the spread of the electron cloud as a function of time. The longer the drift time, the more the electron cloud diffuses and lower signal amplitude and wider width are measured. The spread of the electron cloud as a function of drift time is given by:

$$\sigma_{x,y}(t) = \sqrt{\sigma_{0,x,y}^2 + 2Dt} \qquad \textbf{(4.9)}$$

where "$\sigma_{0,x,y}$" corresponds to the initial size of the electron cloud and "*D*" is the effective diffusion constant. The diffusion constant is calculated to be approximately *3.0-3.5* $\mu m^2/ns$ at room temperature [ref. 4.4, 4.5].

Considering a constant integrated charge, i.e. no charge recombination effect, the amplitude of the signal can be approximated to be the total charge divided by the cloud area ($\sigma_x \times \sigma_y$). With that approximation, the signal amplitude depends on the inverse of the drift time. Figure 4.17 shows the integrated signal amplitude, measured on one anode, as a function of the drift distance. The solid line represents a fitted curve using a function of the type:

$$A(x) = \frac{a}{b + c \cdot x} \qquad \textbf{(4.10)}$$

Recombination effects would contribute with an exponential decay factor. Due to the fact that the signal is read through a pre-amplifier/shaper circuit, an absolute calculation of the amplitude decay is not trivial. However, the relatively good agreement between the adjusted curve and the signal amplitude measurement, indicates that recombination effects are small. Actual measurements from experiment E896, which will be shown in chapter 7, measuring the complete integrated signal from several anodes, also show no evidence of charge loss due to recombination effects.

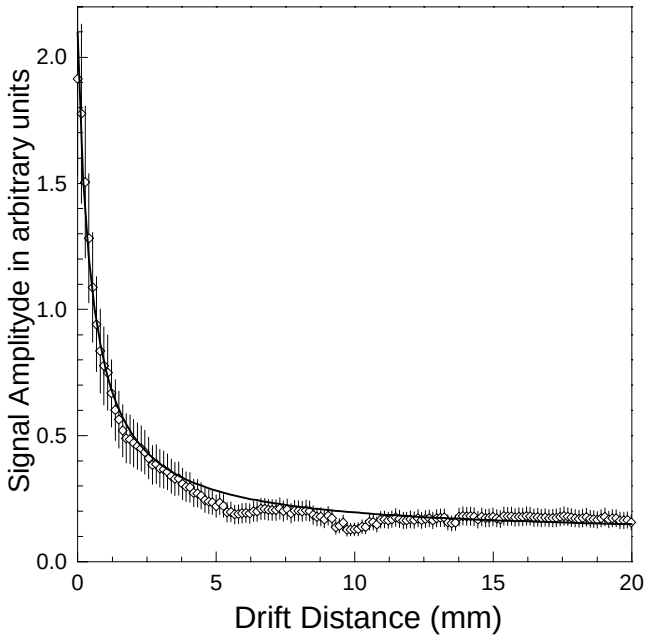

Figure 4.17: *Measured signal amplitude from one anode, as a function of drift distance.*

4.4.1.2 Signal width in the drift direction

The width of the electron cloud as a function of the drift time is given by equation 4.9. The Coulomb repulsion increases the initial cloud size (σ_0) and, in general, it also affects the time dependence, $\sigma(t)$. However, for low ionization ($Q_0 \leq 2 \cdot 10^{14}$), the Coulomb repulsion contribution is small, and it can be incorporated in the first term of equation 4.11.

Figure 4.18 shows the squared value of the measured signal width (σ^2) as a function of the drift time. This data was taken using a laser signal on the test station. The measurement shows the linear dependence of σ^2 on the drift time. The value of the measured signal width (σ) corresponds to the width of the electron cloud folded with the response function of the readout electronics, mainly the shaper. In addition, due to the nonzero spatial size and time duration of the laser

hit, the electron cloud initially has a nonzero size. For these reasons, it is not possible to determine in a simple manner the diffusion constant (D) from this measurement.

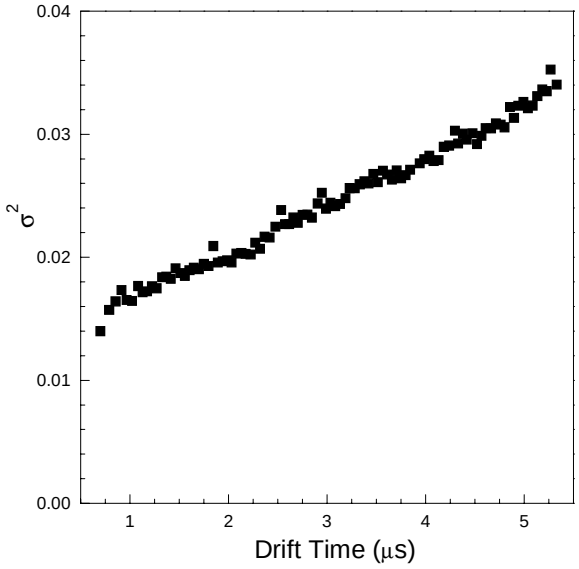

Figure 4.18: *Square of the measured signal width (σ^2) as a function of drift time.*

4.4.1.3 Signal width in the transverse direction

The lateral spread of the electron cloud is shown on figure 4.19. Assuming a gaussian shaped distribution of charge and considering that the recombination effect is small, it is possible to calculate the diffusion constant "D" using equation 4.12. The measurement shown in figure 4.19 yield a diffusion constant of approximately *5.1* $\mu m^2/ns$, larger than the expected *3.5* $\mu m^2/ns$. The difference could be due to the contribution of the Coulomb repulsion, which is forcing the electron cloud to expand more rapidly, thus increasing the effective diffusion constant. In addition, small impurities in the silicon lattice, and non-linearities in the voltage distribution generate scattering points that could contribute to the spreading of the electron cloud. On the other hand, the small difference between

the measurement and the expected value shows that the drift non-linearities and impurities of the silicon lattice are small.

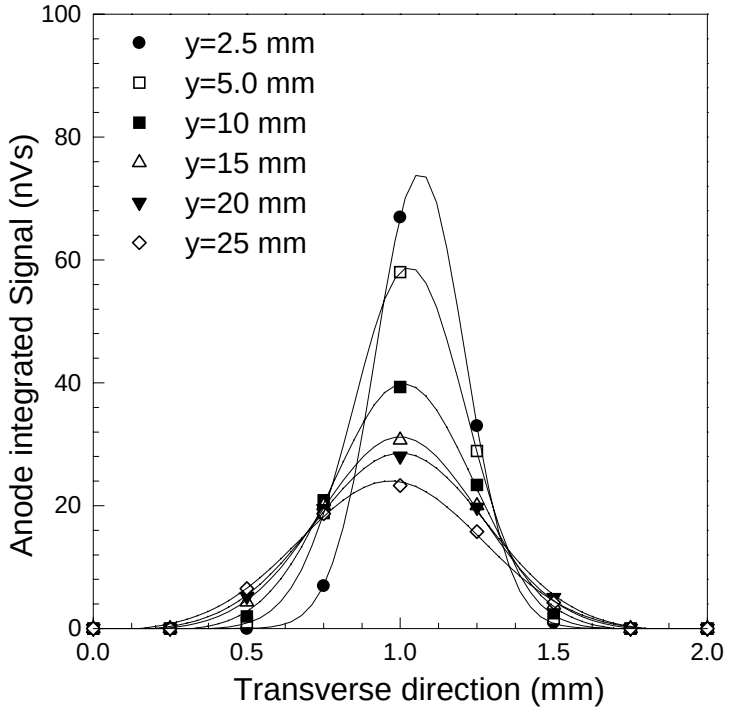

Figure 4.19: *Lateral distribution of the electron cloud measured across several anodes. Y corresponds to the drift distance.*

4.4.2 Position accuracy in the drift direction

The position accuracy is defined as the degree of conformity of the position measurement to a true value. The detector position accuracy depends only on the intrinsic characteristics of the detector, whereas the position resolution is defined as the smallest distance to which the detector is sensitive, i.e. it is the smallest distance that can be distinguished with the detector considering hits of independent events. The double hit resolution is defined as the smallest distinguishable distance between two hits of the same event. The double hit resolution is an important parameter when considering tracking detectors in high

hit density environments. The position accuracy affects directly the position resolution and the double hit resolution, however, the position resolution also depends on the size of the sampling pixel and on the size of the electron cloud.

The position accuracy in the drift direction was obtained by taking a series of drift measurements with the laser at a fixed position. The laser intensity was kept sufficiently high for the output signal to be considerably higher than the noise but, sufficiently low to not saturate the electronics. Also, it was assumed that the size of the laser spot was small (diameter < *25 μm*) and that the charge distribution had a gaussian-type shape. The sampling pixel size in the time direction was kept small compared to the signal width (~2ns). Figure 4.20 shows the distribution of the position measurement for three different drift distances.

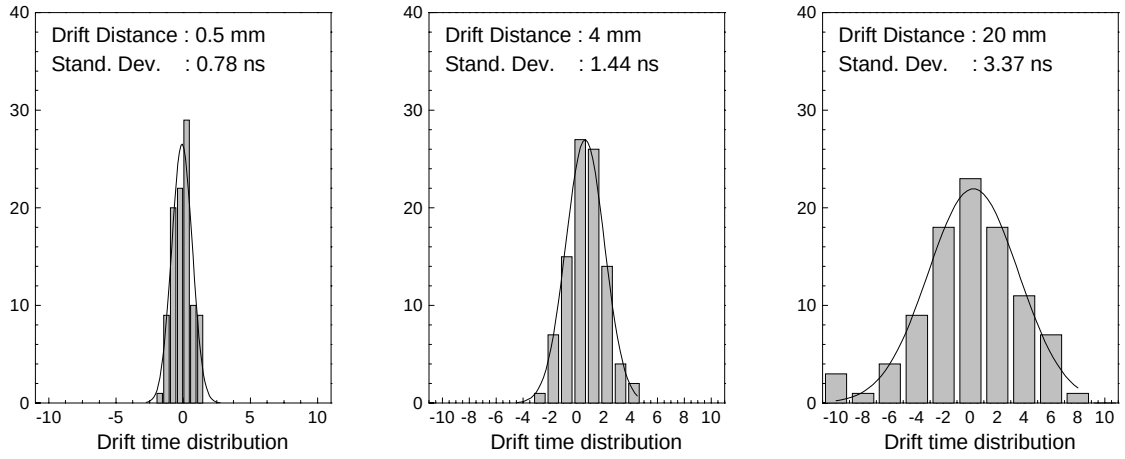

Figure 4.20: *Scatter in the drift time measurement for three different drift distance. For each position, the measurement was sampled 100 times.*

Based on figure 4.20, we conclude that there is a small degradation of the position accuracy for higher drift distances. The accuracy should not depend on the drift distance, because it is defined as an intrinsic parameter of the detector, however the changes indicate that there is still some systematic effect in the measurement. Position accuracy for the shortest drift distance corresponds to the intrinsic position accuracy of the detector. *0.78 ns* at full drift field of *6.2 μm/ns*

(*500 V/cm*) translates to a position accuracy of approximately *5 μm*. The standard deviation of the drift time measurement at the maximum drift distance sets the minimum position accuracy achievable with the detector. Therefore, the position accuracy is better than *3.5 ns*, which corresponds to approximately *22 μm* at full drift field.

4.4.3 Drift non-linearity

Voltage non-linearities and irregularities in the silicon lattice can cause drift non-linearities. Non-linearities due to voltage variations will be equal across the detector. On the other hand, non-linearities caused by defects in the silicon lattice are localized and can be different for each anode.

With the laser set-up described earlier in this chapter, drift non-linearity curves were measured across the detector. Figure 4.21 shows a typical drift time measurement as a function of the drift distance for two different detector biases. In both cases, there is an obvious change in the drift velocity at a drift distance of approximately *2.7 mm*, represented by the change in the slope of the drift curve. This is caused by the voltage difference between the n-side and the p-side of the focusing region of the detector (between cathode 20 and the anodes). This voltage difference is necessary to direct the electron cloud from the detector center plane towards the n-side surface where the collection anodes are placed. The change in drift velocity is well known and constant in time and therefore easy to calibrate. Figure 4.22 shows the non-linearity of the drift curve measured at *HV=-1500V*, with respect to a linear fit to the data above a drift distance of *3mm*. Figure 4.23 shows a histogram of the corresponding drift non-linearity. In this example, the non-linearity has a standard deviation of approximately *3.1ns*.

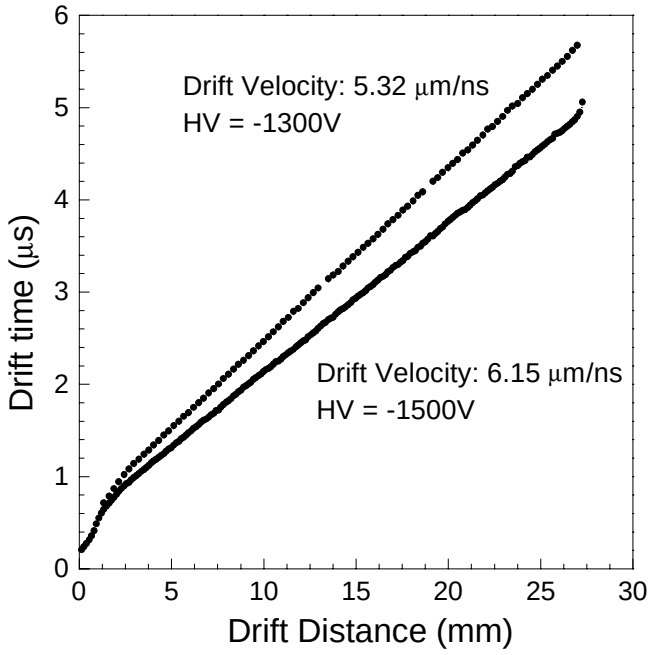

Figure 4.21: *Drift time as a function of drift distance, measured at the laser test station for two detector bias values.*

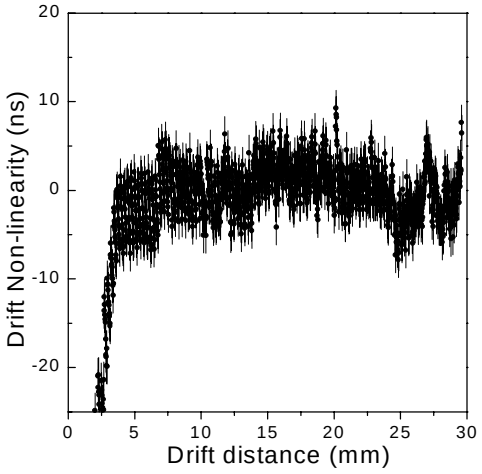

Figure 4.22: *Drift non-linearity as a function of drift distance.*

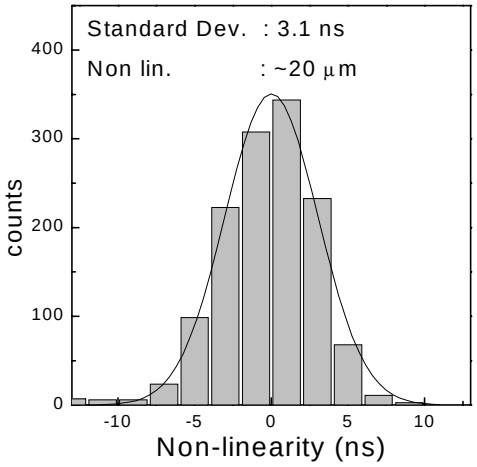

Figure 4.23: *Histogram of the drift non-linearity.*

Localized defects in the silicon lattice can be detected through the measurement of a variety of parameters such as anode leakage currents. Therefore, it is possible to choose satisfactory detectors that have negligible defects based on the anode leakage current measurements. In a wide sample of non-linearity measurements performed on various detectors, it was determined that most of the drift non-linearities are uniform across the anodes. In that case, a non-uniformity measurement from a single anode is sufficient to "map" the detector and improve the position resolution.

In summary, the intrinsic position accuracy that can be achieved with the tested drift detectors is better than $20\ \mu m$.

The double hit resolution depends not only on the position accuracy of the detector, but also on the size of the electron cloud. For hits generated by minimum ionizing particles, and a position accuracy of $20\ \mu m$, the double particle resolution for the STAR drift detector was calculated to be approximately $600\ \mu m$ for the maximum drift distance. At shorter drift distances, two hits can be resolved down to $400\ \mu m$. Details of these calculations as well as improvements on the double hit resolution based on offline waveform analysis are described in reference 4.6.

4.5 Temperature dependence

The electron mobility of silicon at room temperature is approximately $150\ \mu m^2/V\text{-}s$. However, for mono-polar semiconductors, such as silicon and Germanium, vibration of the lattice (acoustic phonon excitation) as well as ionized impurities result in scattering of the electrons which significantly affects the mobility constant. The vibration of the lattice is dependent on the temperature. Therefore:

$$\mu_l \approx \left(m^*\right)^{-5/2} T^{-3/2} \tag{4.13}$$

where μ_l is the mobility component that is affected by the lattice vibrations and m^* is the electron effective mass. The variation of mobility due to ionized impurities (μ_i) can be described by:

$$\mu_i \approx \left(m^*\right)^{-1/2} N_I^{-1} T^{3/2} \tag{4.14}$$

where N_I is the ionized impurity density. The combined mobility is given by:

$$\mu = \left(\frac{1}{\mu_l} + \frac{1}{\mu_i} \right)^{-1} \propto T^{-\alpha} \tag{4.15}$$

Near room temperature, the mobility varies as $T^{-2.42}$ for *n*-type silicon and $T^{-2.20}$ for *p*-type silicon.

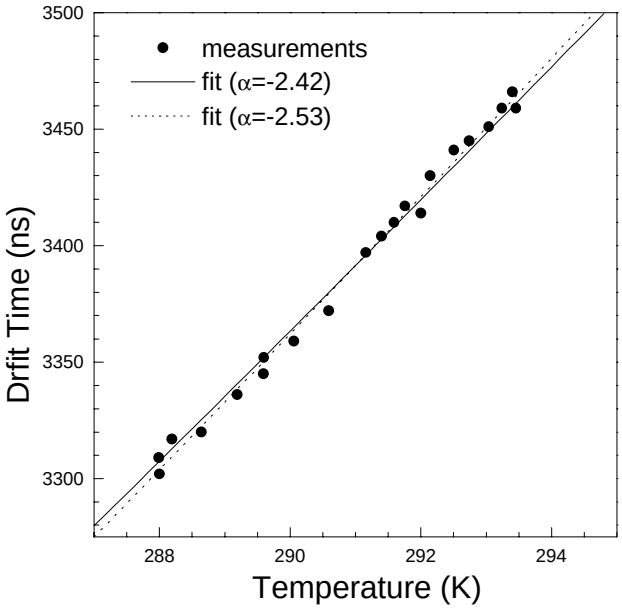

Figure 4.24: *Drift time as a function of temperature.*

Using laser injection, the drift velocity dependence on the temperature was measured. The laser was kept fixed at a drift distance of approximately *1.2 cm* from the anodes. The temperature was measured with a thermistor near the detector surface. Results are shown in figure 4.24. The least minimum square fit, shown as the dotted curve, gives a value of α*=-2.53*. The solid line shows the calculated curve for α*=-2.42*, the theoretical value for the electron mobility in an ideal case. The difference between the two curves is negligible. It can be attributed to several effects such as small drift non-linearity, which affects the drift time measurement or an offset of the absolute temperature between the measuring point and the silicon itself.

Due to the high position resolution that can be achieved with this detector, the temperature effect cannot be neglected. From the dependence of the electron mobility on the temperature, the drift velocity variation can be written as:

$$\frac{dv_{drift}}{v_{drift}} = -\alpha \cdot \frac{dT}{T} \qquad \textbf{(4.20)}$$

Based on equation 4.20, a temperature variation of *1K* corresponds to a drift velocity change of almost *1%*. For a full drift of *3 cm*, with a drift velocity of *6*μ*m/ns* this temperature variation would correspond to a position offset of *244*μ*m*.

To maintain the position resolution of approximately *25*μ*m* achievable with this detector, the temperature would have to be kept constant in within *0.1K*. Since that is impractical in an experimental environment, calibration of the drift velocity is necessary, which is accomplished using charge injection lines placed in known positions across the detector. The calibration line design and performance will be discussed in detail in the following chapter.